SCIENCE CHINA
Technological Sciences

Special Topic: Advances in Numerical Manifold Method
•Article•

April 2024 Vol.67 No.4: 1007–1022
https://doi.org/10.1007/s11431-022-2321-9

Three-dimensional numerical manifold method for heat conduction problems with a simplex integral on the boundary

TONG DeFu[1,2,3], YI XiongWei[3], TAN Fei[1*], JIAO YuYong[1*] & LIANG JiaWei[1]

[1] *Faculty of Engineering, China University of Geoscience, Wuhan 430074, China;*
[2] *Department of Civil Engineering, Monash University, Melbourne VIC 3800, Australia;*
[3] *Badong National Observation and Research Station of Geohazards, China University of Geoscience, Wuhan 430074, China*

Received October 29, 2022; accepted January 17, 2023; published online November 1, 2023

The three-dimensional numerical manifold method (3D-NMM), which is based on the derivation of Galerkin's variation, is a powerful calculation tool that uses two cover systems. The 3D-NMM can be used to handle continue-discontinue problems and extend to THM coupling. In this study, we extended the 3D-NMM to simulate both steady-state and transient heat conduction problems. The modelling was carried out using the raster methods (RSM). For the system equation, a variational method was employed to drive the discrete equations, and the crucial boundary conditions were solved using the penalty method. To solve the boundary integral problem, the face integral of scalar fields and two-dimensional simplex integration were used to accurately describe the integral on polygonal boundaries. Several numerical examples were used to verify the results of 3D steady-state and transient heat-conduction problems. The numerical results indicated that the 3D-NMM is effective for handling 3D both steady-state and transient heat conduction problems with high solution accuracy.

three-dimensional numerical manifold method, transient analysis, heat conduction problem, Galerkin variation, simplex integration

Citation: Tong D F, Yi X W, Tan F, et al. Three-dimensional numerical manifold method for heat conduction problems with a simplex integral on the boundary. Sci China Tech Sci, 2024, 67: 1007–1022, https://doi.org/10.1007/s11431-022-2321-9

1 Introduction

With increasing socioeconomic development, various large-scale engineering projects have been conducted worldwide. In particular, deep underground geotechnical projects [1,2], such as nuclear waste storage and geothermal energy development, are constructed in complex engineering geological environments. These projects are susceptible to the effects of high temperatures and high *in-situ* stresses. The conduction of heat inside a rock mass can lead to changes in the stress state of the rock mass [3–5], thereby severely affecting the construction and safety stability of underground projects. Therefore, further research is required to address problems associated with steady-state heat conduction (SSHC) problems and transient heat conduction (TRHC) problems. The findings of the present study can help improve the stability of rocks at high temperatures.

Most methods for solving differential equations or partial differential equations under boundary conditions can be applied to analyse the internal temperature field of a rock mass. However, deriving analytical solutions for the temperature distribution in rock mass in practical engineering applications is challenging because of the complexity of specific conditions such as boundary conditions and partial differential equations [6].

Recently matured computer technology and advanced numerical methods are effective means for heat conduction analysis. Several researchers have used the finite element

*Corresponding authors (email: tanfei@cug.edu.cn; yyjiao@cug.edu.cn)

method (FEM), finite difference method (FDM), boundary element method (BEM), etc., to derive temperature field solutions. Using the FEM combined with the weighted residual method, Brunch and Zyvoloski [7] simulated the transient heat transfer problem with high stability and convergence accuracy. Reddy and Gartling [8] applied the FEM to TRHC problems and proposed corresponding solutions and treatment methods. Improving upon the Douglas and Rachford method, Brian [9] proposed an FDM for solving 3D TRHC problems to achieve high-order time scale accuracy. Wang [10] combined the FDM with the maximum principle for differential equations to derive the upper and lower solutions under TRHC conditions. For cylindrical heat conduction problems, Li et al. [11] developed a unique finite volume method (FVM) based on local analytical solutions and compared its results with those of the conventional second-order FVM. The results indicated that the proposed method had higher computing efficiency and accuracy. To verify the computational effectiveness and accuracy, Liu and Cheng [12] developed a weak variant of the 3D TRHC problem based on an improved moving least squares method. Wrobel and Brebbia [13] applied the BEM to SSHC and TRHC problems and used it to solve complex engineering heat conduction problems. Furthermore, Gao [14] introduced a straightforward boundary-domain integral equation to solve heat conduction problems including those related to heat production and nonhomogeneous thermal conductivity.

Although the forementioned numerical methods can effectively solve heat conduction problems, denser grids should be meshed and remeshed to achieve accuracy in solving problems related to inclusions, discontinuous deformation problems and crack expansion.

Numerical manifold method (NMM) [15,16] is a new calculation method proposed by Shi [15] in 1991 following the block theory and discontinuous deformation analysis (DDA), which innovatively introduces the concept of finite cover in topological and differential manifolds into numerical calculation, such that the method can naturally handle issues with both continuous and discontinuous deformation. After nearly three decades of development, the NMM is primarily applied to solve problems associated with crack extension [17–19], P adaptive analysis [20], heat conduction [1], thermal fracture [21], hydraulic fracturing [22], and soil rock mixtures [23,24]. In terms of heat conduction, which is currently constrained to the two-dimensional(2D) domain, He et al. [25,26] extended the NMM to transient heat transfer models of granular materials and simulated the heat transfer between microscopic rock particles by inserting thermally conductive bonding units between Voronoi polygons. Subsequently, the contact algorithm of the NMM was improved based on the zero-thickness cohesive element model to simulate the damage process of granular materials under the action of thermal coupling. Zhang et al. [6,27,28] used the NMM with a hexagonal mathematical grid and proposed a solution strategy for the time-varying global equations and a spatial integration scheme to solve the 2D transient heat conduction problem, and the thermal stress intensity factor was calculated by coupling the temperature and force fields. The Galerkin variational method was used to derive the TRHC governing equations for materials with functional gradients, and the accuracy of the procedure was verified through numerical calculations. Using the traditional two-point difference method for discretization in the time domain and the complex variable moving least squares method for discretization in space, Gao and Wei [29] established the governing equations for transient heat transfer based on the complex variable meshless manifold method. Zhang et al. [30] used the MLS-based NMM to deal with the nonlinear transient heat conduction problems, and believed the proposed method has the advantages of both MLS and NMM.

Several studies have reported the application of NMM to 2D heat conduction problems; however, few studies have focused on 3D heat conduction problems. Therefore, we established a shape function based on the hexahedral finite cover systems, and a governing equation for the 3D-NMM was established by the Galerkin variational method. Furthermore, the boundary conditions and variational problems of the 3D steady-state and transient temperature fields were derived using the basic differential equations. For the problem that the exact integration of the boundary was not easy to handle, the exact integration of the polygonal boundary of the 3D block was carried out by the face integral of the scalar field and the 2D simplex integral.

2 A brief introduction to 3D NMM

The NMM contains two cover systems (CSs) which are the mathematical cover (MC) systems and the physical cover (PC) systems. Thus, the NMM can easily simulate continuous and discontinuous problems in a unified framework. Few studies have focused on 3D-NMM and no pre-processing tools are readily available. This section discusses the basic concepts of 3D-NMM and the generation algorithm of 3D manifold elements (MEs) [31].

2.1 Basic concepts of 3D-NMM

Similar to 2D NMM, the MC of 3D-NMM can be freely chosen by the user, and it can be regular or irregular polyhedrons. The ability to cover the entire physical domain is the only prerequisite for MC [32–35]. For the convenience of calculation and solution, the regular FE-meshes are usually used to construct the MC, and all the mathematical patches (MPs) form a union area which is the MC. Here the MPs are

the polyhedrons that have a common node. Using the MPs to cut the physical domain (contains joints, boundaries and material interfaces, and so on), a series of physical patches (PPs) can be generated. In addition, the PC is the union of all PPs. Finally, the overlapping parts of several neighbouring PPs will form a manifold element (ME) which is the basic calculated element.

The generation of 3D MEs mainly includes the generation of MC, PC, and manifold blocks, which involves block identification, block cutting, and updating of the cover system. Figure 1 shows the 3D MEs generation process. In Figure 1(a), corresponding geometric blocks can be generated by auxiliary modelling software or input block data, and through the block identification algorithm to generate the block system and joint information. In Figure 1(b), there is a penetrating fracture inserted into the pyramid body, and the pyramid is divided into two parts. Subsequently, according to the physical domain, the corresponding mathematical grid and MC are generated by the raster method (RSM) [31,32]. Here a standard 2.5×2.5×2.5 hexahedral raster is used as the mathematical meshes, each node in the FE meshes is called a star and use NMMNode index to number them. Furthermore, based on the neighbouring mesh, using the Boolean intersection algorithm to cut the physical domain will create the Manifold blocks. Finally, a pointer data structure is used to relate the manifold blocks to the corresponding MC and PC information. The MC and PC can be seen in Figure 1(c), the numbers of hexahedral meshes to build MC1, MC6, MC14 are 1, 2 and 8. Because each MC was divided into two parts by a joint face, each MC contains two PPs. Finally, the intersection of several PPs forms the MEs, and Figure 1(d) shows a part of MEs generated for this model.

2.2 Framework of 3D-NMM

While the displacement functions of 3D-NMM are defined on PC, and the weight function is defined on MPs [36,37]. Here, the MCs are composed of a series of mathematical patches (MP). On each MP, a weight function $w_i(x,y,z)$ is defined as eq. (1)

$$\left.\begin{aligned} &0 < w_i(x,y,z) \leqslant 1, \quad (x,y,z) \in \Omega_i^m, \\ &w_i(x,y,z) = 0, \qquad (x,y,z) \notin \Omega_i^m, \\ &\sum_{i=1}^{n^p} w_i(x,y,z) = 1, \end{aligned}\right\} \tag{1}$$

where Ω_i^m is the ith mathematical patches (MP), and n^p is the number of MPs which can partially overlap each other. $w_i(x,y,z)$ is the weight function. In present study, the FE-mesh is used as the MC, so the shape function of FEM is equal to $w_i(x,y,z)$. These concepts can be used to build the 3D-NMM approximation function. A cover function $u_i(x,y,z)$ is defined individually as a local approximation on each PC, which can be a constant, linear, high-order polynomial, or other function with unknowns to be determined. Then, the global function $u(x,y,z)$ on each ME is approximated to

$$\{u(x,y,z)\} = \sum_{i=1}^{n} w_i(x,y,z)\{u_i(x,y,z)\}. \tag{2}$$

To make computation easier, basic and regular manifold patterns are recommended in 3D-NMM. In this paper, in order to form the mathematic cover, we choose the hexahedron mesh which is easy to cover the entire 3D space. For heat conduction problems the global approximation $\mathbf{T}^{\mathrm{e}}(x,y,z)$ in each ME in eq. (2) could be rewritten as follows:

$$\mathbf{T}^{\mathrm{e}}(x,y,z) = \sum_{i=1}^{8} w_i(x,y,z) T_i(x,y,z). \tag{3}$$

In this paper, the FE-element is used as the MC, $w_i(x,y,z)$ can be inherited from the shape function of FEM. Note that $\mathbf{T}^{\mathrm{e}}(x,y,z)$ can also be expressed as

$$\mathbf{T}^{\mathrm{e}} = \mathbf{NT}, \tag{4}$$

where **N** and **T** stand for the shape function matrix and nodal temperature vector which are connected to the ME, respectively, and can be written as follows:

$$\mathbf{N} = [\mathbf{N}_1\mathbf{N}_2 \cdots \mathbf{N}_8], \tag{5}$$

$$\mathbf{T} = [\mathbf{T}_1\mathbf{T}_2 \cdots \mathbf{T}_8]^{\mathrm{T}}, \tag{6}$$

where $N_i(x, y, z)$ stands for the 8-node hexahedral element's shape function. Additionally, it can be expressed using the local coordinate system [38].

3 Heat conduction problem based on 3D-NMM

3.1 Problem statement

A significant advantage of NMM is that it is able to handle complex boundary problems or fracture rock masses when it comes to 3D heat conduction problems. Therefore, before performing 3D thermal coupling studies, 3D heat conduction should be analysed comprehensively.

Consider heat conduction [39] in an isotropic homogeneous domain Ω with the boundary $\Gamma = \Gamma_{S_1} \cup \Gamma_{S_2} \cup \Gamma_{S_3}$ as shown in Figure 2. The temperature is unaffected by time in the 3D SSHC problem. The governing partial differential equation for the 3D SSHC problem can be written as follows:

$$k\frac{\partial^2 T}{\partial x^2} + k\frac{\partial^2 T}{\partial y^2} + k\frac{\partial^2 T}{\partial z^2} + Q = 0. \tag{7}$$

The primary difference between SSHC and TRHC problems is that transient problems are related to time. The

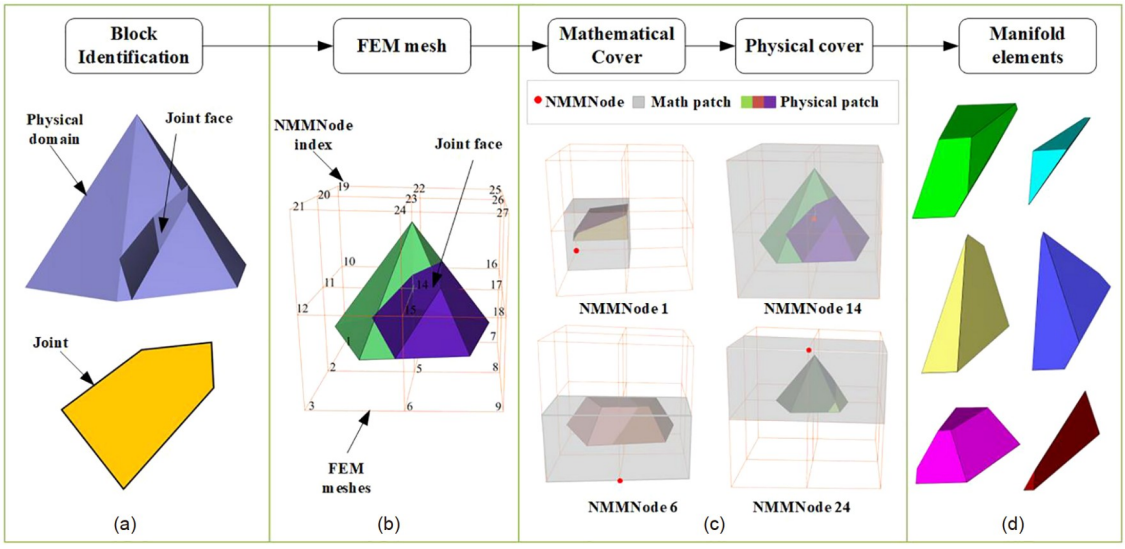

Figure 1 Process of generating manifold elements for 3D- NMM.

governing partial differential equation for the 3D TRHC problem can be written as follows:

$$k\frac{\partial^2 T}{\partial x^2}+k\frac{\partial^2 T}{\partial y^2}+k\frac{\partial^2 T}{\partial z^2}+Q=\rho c\frac{\partial T}{\partial t}. \tag{8}$$

Here are the boundary conditions:

$$T=T_1, \text{on } \Gamma_{S_1}, \tag{9}$$

$$k\frac{\partial T}{\partial x}n_x+k\frac{\partial T}{\partial y}n_y+k\frac{\partial T}{\partial z}n_z=q, \text{on } \Gamma_{S_2}, \tag{10}$$

$$k\frac{\partial T}{\partial x}n_x+k\frac{\partial T}{\partial y}n_y+k\frac{\partial T}{\partial z}n_z=h(T_a-T), \text{on } \Gamma_{S_3}. \tag{11}$$

The initial conditions for TRHC are as follows:

$$T=T_0, \tag{12}$$

where T is the temperature of the domain; t is time; Q is the density of the heat source; k is the thermal conductivity; n_x, n_y, n_z are the cosines of the angle between the surface normal vector and the coordinate axis; c is specific heat; ρ is the material density; q is heat flux density; T_1 is the temperature of the boundary Γ_{S_1}; h is the surface heat release coefficient; T_a is the temperature of the boundary Γ_{S_3}; T_0 is the initial temperature value in the area, and $\frac{\partial T}{\partial t}$ is the derivative of the temperature with respect to time.

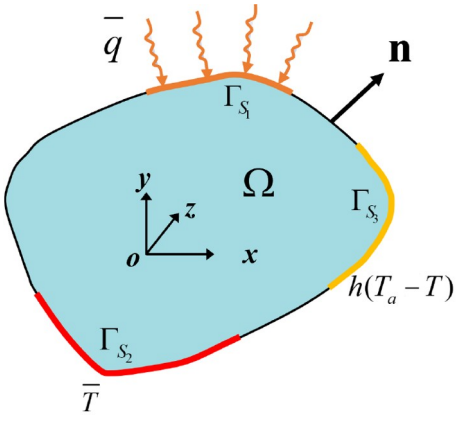

Figure 2 Heat conduction in a domain.

3.2 Derivation of system equations

A Galerkin weighted residual value method was used to derive the governing equation. Using the corresponding conversion, boundary conditions can be included in the functional. The following modified functional are available.

For SSHC problems:

$$I(u)=-\int_\Omega\left[\frac{\partial N_e}{\partial x}\left(k\frac{\partial T}{\partial x}\right)+\frac{\partial N_e}{\partial y}\left(k\frac{\partial T}{\partial y}\right)+\frac{\partial N_e}{\partial z}\left(k\frac{\partial T}{\partial z}\right)-N_eQ\right]\mathrm{d}\Omega+\int_{\Gamma_{S_2}}N_eq\,\mathrm{d}s+\int_{\Gamma_{S_3}}N_eh(T_a-T)\mathrm{d}s. \tag{13}$$

For TRHC problems:

$$I(u)=-\int_\Omega\left[\frac{\partial N_e}{\partial x}\left(k\frac{\partial T}{\partial x}\right)+\frac{\partial N_e}{\partial y}\left(k\frac{\partial T}{\partial y}\right)+\frac{\partial N_e}{\partial z}\left(k\frac{\partial T}{\partial z}\right)-N_eQ+N_e\rho c\frac{\partial T}{\partial t}\right]\mathrm{d}\Omega+\int_{\Gamma_{S_2}}N_eq\,\mathrm{d}s+\int_{\Gamma_{S_3}}N_eh(T_a-T)\mathrm{d}s. \tag{14}$$

The extreme values of the variation problem $I(u)$ related to the boundary problem solution are shown below.

For SSHC problems:

$$\begin{cases} F(u)=\int_{\Omega}\left\{\frac{1}{2}k(\nabla T)^2+Q\right\}\mathrm{d}\Omega \\ \qquad +\int_{\Gamma_{S_2}}\bar{q}T\mathrm{d}s+\int_{\Gamma_{S_3}}h\left(\frac{1}{2}T^2-TT_a\right)T\mathrm{d}s, \\ T\Big|_{\Gamma_{S1}}=T_1, \\ \delta F(u)=0. \end{cases} \tag{15}$$

For TRHC problems:

$$\begin{cases} F(u)=\int_{\Omega}\left\{\frac{1}{2}k(\nabla T)^2+Q-\rho c\frac{\partial T}{\partial t}\right\}\mathrm{d}\Omega \\ \qquad +\int_{\Gamma_{S_2}}\bar{q}T\mathrm{d}s+\int_{\Gamma_{S_3}}h\left(\frac{1}{2}T^2-TT_a\right)T\mathrm{d}s, \\ T\Big|_{\Gamma_{S_1}}=T_1, \\ \delta F(u)=0. \end{cases} \tag{16}$$

Several methods can be used to deal with the first type of boundary condition in heat conduction problems, for example, the penalty function method. In comparison with Lagrange multipliers, the penalty function method has the advantage of being easy and quick to operate. The value of the penalty has a significant effect on the calculation results. Theoretically, the larger the penalty value, the more accurate the calculation result, but too large a penalty value leads to pathologies in the system of equations and matrices. Therefore, the penalty value is chosen according to the following [40]:

$$\lambda=10^4\times\max\left(\left|K_{ij}\right|\right),1\leqslant i\leqslant n,1\leqslant j\leqslant n, \tag{17}$$

where λ is the penalty value, K_{ij} is the stiffness submatrix, and n is the total degrees number of freedom for the system equation.

A modified function for the 3D TRHC problems is as follows:

$$\begin{aligned} &F^*(u)= \\ &\int_{\Omega}\left[\frac{\partial N_e}{\partial x}\left(k\frac{\partial T}{\partial x}\right)+\frac{\partial N_e}{\partial y}\left(k\frac{\partial T}{\partial y}\right)+\frac{\partial N_e}{\partial z}\left(k\frac{\partial T}{\partial z}\right)N_eQ-\rho c\frac{\partial T}{\partial t}\right]\mathrm{d}\Omega \\ &+\int_{\Gamma_{S_1}}N_e\lambda N_e\mathrm{d}s-\int_{\Gamma_{S_2}}N_eq\mathrm{d}s+\int_{\Gamma_{S_3}}N_eh(T_a-T)\mathrm{d}s \\ &=\int_{\Omega}\left[\frac{\partial N_e}{\partial x}\left(k\frac{\partial T}{\partial x}\right)+\frac{\partial N_e}{\partial y}\left(k\frac{\partial T}{\partial y}\right)+\frac{\partial N_e}{\partial z}\left(k\frac{\partial T}{\partial z}\right)\right]\mathrm{d}\Omega \\ &\quad+\int_{\Gamma_{S_1}}N_e\lambda N_e\mathrm{d}s+\int_{\Gamma_{S_3}}N_ehN_e\mathrm{d}s+\int_{\Omega}N_eQ\mathrm{d}\Omega \\ &\quad-\int_{\Gamma_{S_2}}N_eq\mathrm{d}s+\int_{\Gamma_{S_3}}N_ehT_a\mathrm{d}s-\int_{\Omega}N_e\rho c\frac{\partial T}{\partial t}\mathrm{d}\Omega. \end{aligned} \tag{18}$$

From weak-form equation, we obtain algebraic system equations by dividing the solution domain into manifolds, and by using manifold element shape functions, the solutions within elements can be determined based on the values of nodes. When a transient temperature field is considered, its time derivative is given by the shape function, and its time domain is discretized by using the backward difference method, which is expressed as follows:

$$\Delta T_n=T_{n+1}-T_n=\Delta t_n\left(\frac{\partial T}{\partial t}\right)_{n+1}. \tag{19}$$

The rate of change in temperature at any position can be derived using the following formula:

$$\frac{\partial T}{\partial t}=N_e\frac{\partial T_e}{\partial t}. \tag{20}$$

The temperature field value was calculated by substituting eq. (14) into the fundamental equation to solve transient heat conduction.

$$\sum_e\left[\left(\mathbf{K}^e+\frac{\mathbf{H}^e}{\Delta t_n}\right)\mathbf{T}_{n+1}^e-\frac{\mathbf{H}^e}{\Delta t_n}\mathbf{T}_n^e\right]=\sum_e\mathbf{F}^e. \tag{21}$$

The overall calculation matrix was formed by superimposing the calculation matrices of each ME shown above. The following formula was used

$$\left(\mathbf{K}+\frac{\mathbf{H}}{\Delta t}\right)\mathbf{T}_{n+1}=\mathbf{F}+\frac{\mathbf{H}}{\Delta t}\mathbf{T}_n, \tag{22}$$

where Δt is the time step of transient calculation; $\mathbf{T}_n$ is the temperature value obtained in the nth step; $\mathbf{T}_{n+1}$ is the temperature value calculated in the (n+1)th step. $\mathbf{K}$ is the temperature stiffness matrix; $\mathbf{F}$ is the temperature load matrix; $\mathbf{H}$ is the heat capacity matrix.

In which,

$$\mathbf{K}=\sum_{i=1}^{n}\mathbf{K}^e+\sum_{i=1}^{n_1}\mathbf{K}_1^e+\sum_{i=1}^{n_3}\mathbf{K}_3^e, \tag{23-1}$$

$$\mathbf{H}=\sum_{i=1}^{n}\mathbf{H}^e, \tag{23-2}$$

$$\mathbf{F}=\sum_{i=1}^{n}\mathbf{F}_{\Omega}^e+\sum_{i=1}^{n_1}\mathbf{F}_1^e-\sum_{i=1}^{n_2}\mathbf{F}_2^e+\sum_{i=1}^{n_3}\mathbf{F}_3^e. \tag{23-3}$$

Here,

$$\left.\begin{aligned} \mathbf{K}^e&=\int_{\Omega^e}\mathbf{B}^{\mathrm{T}}k\,\mathbf{B}\mathrm{d}\Omega, \\ \mathbf{K}_1^e&=\int_{\Gamma_{S_1}^e}\mathbf{\Phi}^{\mathrm{T}}\lambda\mathbf{\Phi}\mathrm{d}\Gamma_{S_1}, \\ \mathbf{K}_3^e&=\int_{\Gamma_{S_3}^e}\mathbf{\Phi}^{\mathrm{T}}h\mathbf{\Phi}\mathrm{d}\Gamma_{S_3}, \end{aligned}\right\} \tag{24-1}$$

$$\mathbf{H}^e=\int_{\Omega^e}\mathbf{\Phi}^{\mathrm{T}}\mathbf{\Phi}\rho c\mathrm{d}\Omega, \tag{24-2}$$

$$\left.\begin{aligned} \mathbf{F}^e&=\int_{\Omega^e}\mathbf{\Phi}^{\mathrm{T}}Q\mathrm{d}\Omega, \\ \mathbf{F}_1^e&=\int_{\Gamma_{S_1}^e}\mathbf{\Phi}^{\mathrm{T}}\lambda\mathbf{T}_1\mathrm{d}\Gamma_{S_1}, \\ \mathbf{F}_2^e&=\int_{\Gamma_{S_2}^e}\mathbf{\Phi}^{\mathrm{T}}q\,\mathrm{d}\Gamma_{S_2}, \\ \mathbf{F}_3^e&=\int_{\Gamma_{S_3}^e}\mathbf{\Phi}^{\mathrm{T}}h\mathbf{T}_a\mathrm{d}\Gamma_{S_3}, \end{aligned}\right\} \tag{24-3}$$

where Ω^e is the integral region of a ME; Ω is the integral over the physical domain of the problem; $\Gamma_{S_1}^e$, $\Gamma_{S_2}^e$, $\Gamma_{S_3}^e$ are the different boundaries related to MEs, respectively; n_1, n_2, n_3 is the number of MEs corresponding to the different boundary conditions; $\mathbf{K}^e$, $\mathbf{K}_1^e$, $\mathbf{K}_3^e$ are the element temperature stiffness matrices for different boundary conditions; $\mathbf{F}^e$, $\mathbf{F}_1^e$, $\mathbf{F}_2^e$, $\mathbf{F}_3^e$ are the temperature load vector matrices for different boundaryconditions and $\mathbf{H}^e$ is the heat capacity matrix of the MEs.

For each ME, taking hexahedron elements as the MCs, matrix $\mathbf{B}_e$ is expressed as follows:

$$\mathbf{B}_e=\begin{bmatrix}\frac{\partial W_{e0}}{\partial x} & \frac{\partial W_{e1}}{\partial x} & \frac{\partial W_{e2}}{\partial x} & \cdots & \frac{\partial W_{e7}}{\partial x}\\ \frac{\partial W_{e0}}{\partial y} & \frac{\partial W_{e1}}{\partial y} & \frac{\partial W_{e2}}{\partial y} & \cdots & \frac{\partial W_{e7}}{\partial y}\\ \frac{\partial W_{e0}}{\partial z} & \frac{\partial W_{e1}}{\partial z} & \frac{\partial W_{e2}}{\partial z} & \cdots & \frac{\partial W_{e7}}{\partial z}\end{bmatrix}, \tag{25}$$

$$\mathbf{\Phi}=[W_{e0}W_{e1}W_{e2}W_{e3}W_{e4}W_{e5}W_{e6}W_{e7}], \tag{26}$$

where W_{e0}–W_{e7} are the weight functions of the MEs, and $\mathbf{\Phi}$ is the weight function matrix.

3.3 Simplex integration on the boundary

Tetrahedra are the only shape that can be used for a 3D simplex integration, while triangles are the only shape that can be used for a 2D simplex integration. The integral in eq. (24) is not specific or precise for the polygonal boundary in 3D space in 3D-NMM which involves surface integral and volume integral. To solve this problem, the 3D polygon is projected onto a coordinate plane in this section. Therefore, the integral on a 3D polygon can be computed using a 2D simplex integration [41,42].

In 3D space, assume there have a plane in which a surface integral boundary is located and the equation of the plane can be expressed as

$$\mathbf{A}x+\mathbf{B}y+\mathbf{C}z+D=0. \tag{27}$$

It is assumed that there are n_v vertices on the convex boundary polygon and $\mathbf{[A,B,C]}=[\mathbf{n_x},\mathbf{n_y},\mathbf{n_z}]$ is the outward unit normal vector. According to the formula for integration of surfaces of the first type, a vector can be represented by two other vectors satisfying the following equation:

$$z(x,y)=-\frac{(x-x_1)n_x+(y-y_1)n_y}{n_z}+z_1, \tag{28}$$

where the center coordinate of the boundary is (x_1,y_1,z_1). Taking the *xoy* plane as an example, the integral formula is projected onto the *xoy* plane and the conversion formula is

$$\begin{aligned}&\iint_\Gamma f(x,y,z)\mathrm{d}S\\&=\iint_{\Gamma_{xoy}} f(x,y,z(x,y))\sqrt{1+\left(\frac{\partial z(x,y)}{\partial x}\right)^2+\left(\frac{\partial z(x,y)}{\partial y}\right)^2}\,\mathrm{d}x\mathrm{d}y\\&=\sqrt{1+\left(\frac{n_x}{n_z}\right)^2+\left(\frac{n_y}{n_z}\right)^2}\iint_{\Gamma_{xoy}} f(x,y,z(x,y))\mathrm{d}x\mathrm{d}y,\end{aligned} \tag{29}$$

where $q=\sqrt{1+\left(\frac{n_x}{n_z}\right)^2+\left(\frac{n_y}{n_z}\right)^2}$. On the boundary plane, eq. (24) can be solved using 2D simplex integration [42]. Other planes can be solved according to this method. Thus, eq. (30) is subsequently used to integrate polynomials at the boundary. Additionally, the projected points ought to be organized counterclockwise.

$$S_0=\int 1\mathrm{d}\Gamma=q\iint 1\mathrm{d}x\mathrm{d}y=\frac{q}{2}\sum_{i=1}^{n_v}\begin{vmatrix}x_i & y_i\\ x_{i+1} & y_{i+1}\end{vmatrix}, \tag{30-1}$$

$$\begin{aligned}S_x^b&=S_0x_c^b=\int x\mathrm{d}\Gamma=q\iint x\mathrm{d}x\mathrm{d}y\\&=\frac{q}{6}\sum_{i=1}^{n_v}\begin{vmatrix}x_i & y_i\\ x_{i+1} & y_{i+1}\end{vmatrix}(x_i+x_{i+1}),\end{aligned} \tag{30-2}$$

$$\begin{aligned}S_y^b&=S_0y_c^b=\int y\mathrm{d}\Gamma=q\iint y\mathrm{d}x\mathrm{d}y\\&=\frac{q}{6}\sum_{i=1}^{n_v}\begin{vmatrix}x_i & y_i\\ x_{i+1} & y_{i+1}\end{vmatrix}(y_i+y_{i+1}),\end{aligned} \tag{30-3}$$

$$\begin{aligned}S_{xx}^b&=\int x^2\mathrm{d}\Gamma=q\iint x^2\mathrm{d}x\mathrm{d}y\\&=\frac{q}{12}\sum_{i=1}^{n_v}\begin{vmatrix}x_i & y_i\\ x_{i+1} & y_{i+1}\end{vmatrix}\left(x_i^2+x_{i+1}^2+x_ix_{i+1}\right),\end{aligned} \tag{30-4}$$

$$\begin{aligned}S_{yy}^b&=\int y^2\mathrm{d}\Gamma=q\iint y^2\mathrm{d}x\mathrm{d}y\\&=\frac{q}{12}\sum_{i=1}^{n_v}\begin{vmatrix}x_i & y_i\\ x_{i+1} & y_{i+1}\end{vmatrix}\left(y_i^2+y_{i+1}^2+y_iy_{i+1}\right),\end{aligned} \tag{30-5}$$

$$\begin{aligned}S_{xy}^b&=\int xy\mathrm{d}\Gamma=q\iint xy\mathrm{d}x\mathrm{d}y\\&=\frac{q}{24}\sum_{i=1}^{n_v}\begin{vmatrix}x_i & y_i\\ x_{i+1} & y_{i+1}\end{vmatrix}(2x_iy_i+2x_{i+1}y_{i+1}+x_{i+1}y_i+x_iy_{i+1}),\end{aligned} \tag{30-6}$$

$$\begin{aligned}S_z^b&=S_0z_c^b=\int z\mathrm{d}\Gamma\\&=q\iint\left(-\frac{(x-x_1)n_x+(y-y_1)n_y}{n_z}+z_1\right)\mathrm{d}x\mathrm{d}y\\&=-\frac{n_xS_x^b+n_yS_y^b}{n_z}+\left(z_1+\frac{n_xx_1+n_yy_1}{n_z}\right)S_0,\end{aligned} \tag{30-7}$$

$$\begin{aligned}S_{xz}^b&=\int xz\mathrm{d}\Gamma\\&=q\iint x\left(-\frac{n_xx+n_yy}{n_z}+z_1+\frac{n_xx_1+n_yy_1}{n_z}\right)\mathrm{d}x\mathrm{d}y\end{aligned}$$

$$= -\frac{n_x S_{xx}^b + n_y S_{xy}^b}{n_z} + \left(z_1 + \frac{n_x x_1 + n_y y_1}{n_z}\right) S_x^b, \tag{30-8}$$

$$\begin{aligned} S_{yz}^b &= \int yz \mathrm{d}\Gamma \\ &= q \iint y \left(-\frac{n_x x + n_y y}{n_z} + z_1 + \frac{n_x x_1 + n_y y_1}{n_z}\right) \mathrm{d}x\mathrm{d}y \\ &= -\frac{n_x S_{xy}^b + n_y S_{yy}^b}{n_z} + \left(z_1 + \frac{n_x x_1 + n_y y_1}{n_z}\right) S_y^b, \end{aligned} \tag{30-9}$$

$$\begin{aligned} S_{zz}^b &= \int z^2 \mathrm{d}\Gamma \\ &= q \iint \left(-\frac{(x-x_1)n_x + (y-y_1)n_y}{n_z} + z_1\right)^2 \mathrm{d}x\mathrm{d}y \\ &= -\frac{n_x^2 S_{xx}^b + 2n_x n_y S_{xy}^b + n_y^2 S_{yy}^b}{n_z^2} \\ &\quad -2\left(z_1 + \frac{n_x x_1 + n_y y_1}{n_z}\right)\frac{n_x S_x^b + n_y S_y^b}{n_z} \\ &\quad + \left(z_1 + \frac{n_x x_1 + n_y y_1}{n_z}\right)^2 S_0, \end{aligned} \tag{30-10}$$

$$\begin{aligned} S_{xyz}^b &= \int xyz \mathrm{d}\Gamma \\ &= q \iint xy \left(-\frac{(x-x_1)n_x + (y-y_1)n_y}{n_z} + z_1\right) \mathrm{d}x\mathrm{d}y \\ &= -\frac{n_x S_{x^2y}^b + n_y S_{xy^2}^b}{n_z} + \left(z_1 + \frac{n_x x_1 + n_y y_1}{n_z}\right) S_{xy}^b. \end{aligned} \tag{30-11}$$

The coordinates of the ith vertex are (x_i, y_i, z_i). S_0 represents the area of the boundary polygon, and (x_c^b, y_c^b, z_c^b) represents its centroid.

3.4 Time step setting

The setting of the time step has a notable influence on the entire calculation process. Therefore, a reasonable time step should be selected to ensure high calculation accuracy and solution speed. In this study, the solution time t can be obtained through steady-state calculations, and then Δt can be dynamically adjusted to obtain the optimal solution accuracy and calculation time.

For the TRHC problem, the solution of the governing equation comprised two main parts: the general solution and the particular solution. The particular solution represented the time required for the temperature boundary condition to the stability of the temperature field. It is generally believed that the temperature field reaches a steady state when the general solution tends to 0.

The time t required to reach the steady-state can be solved using eq. (31)

$$\phi(t) = \sum_{i=1}^{N} A_1 \phi_1 \mathrm{e}^{-\omega_1 t} \approx \phi_1 \mathrm{e}^{-\omega_1 t}. \tag{31}$$

In order to reach a steady state, the equation $\mathrm{e}^{-\omega_1 t} \approx 0$ must be satisfied. Approximately consider $\mathrm{e}^{-\omega_1 t} = 0.01$, then $\omega_1 t = 4.6$, that is

$$t = \frac{4.6}{\omega_1}. \tag{32}$$

Hence, we need to find the smallest eigenvalue ω_1. As a result of solving the eigenvalues of ω_1, the time can be calculated using eq. (31). Transient analysis is based on time-step analysis, where $\Delta t = \frac{t}{N}$ is a single time-step and N is the total number of time-steps. In order to avoid unstable results due to extremely small time increments, the Δt needs to satisfy the following equation.

$$\Delta t \geqslant \frac{\rho c}{6k} \Delta l^2, \tag{33}$$

where Δl denotes the size of an ME.

The following equation can be used to determine whether the steady state is reached:

$$\frac{\|\phi_n - \phi_{n-1}\|}{\|\phi_n\|} < ir, \tag{34}$$

where $\|\phi_n - \phi_{n-1}\|$ and $\|\phi_n\|$ denote the parameterization of $\phi_n - \phi_{n-1}$ and ϕ_n, respectively. And ir denotes a small amount (assumed to be 1%). If the value ir is exceedingly small, the equation may not be satisfied, and the computation time may increase exponentially.

Figure 3 illustrates the computational flow of the algorithm proposed in this paper. According to eqs. (31)–(34), we developed a time-step cycle based 3D-NMM calculation program, which contains a preprocessing module, calculation module, and GUI display module.

4 Numerical modelling

4.1 Long-rod heat conduction

To verify the accuracy of 3D-NMM in solving SSHC problems and TRHC problems, a long rod of length 5 m and width and height 0.5 m, respectively, is used as the calculation model. In this model, assuming that the long rod is uniform and isotropic, with k=2.7 W/(m °C), c=0.92 kJ/(kg °C) and ρ = 2.7g/cm^3. The initial temperature of the long rod is uniform ($T(x,y,z) = T_1$). Here, T_1 = 0°C. The boundary conditions are as follows: T_a = 100°C, and T_b = 0°C; the other boundaries are adiabatic. In addition, the model does not contain a heat source. Figure 4(a) and (b) displays the geometric model and the numerical model, respectively. The mesh density is 0.25 m, and a total of 80 meshes are divided to generate 80 MEs. In this manuscript, we use the regular

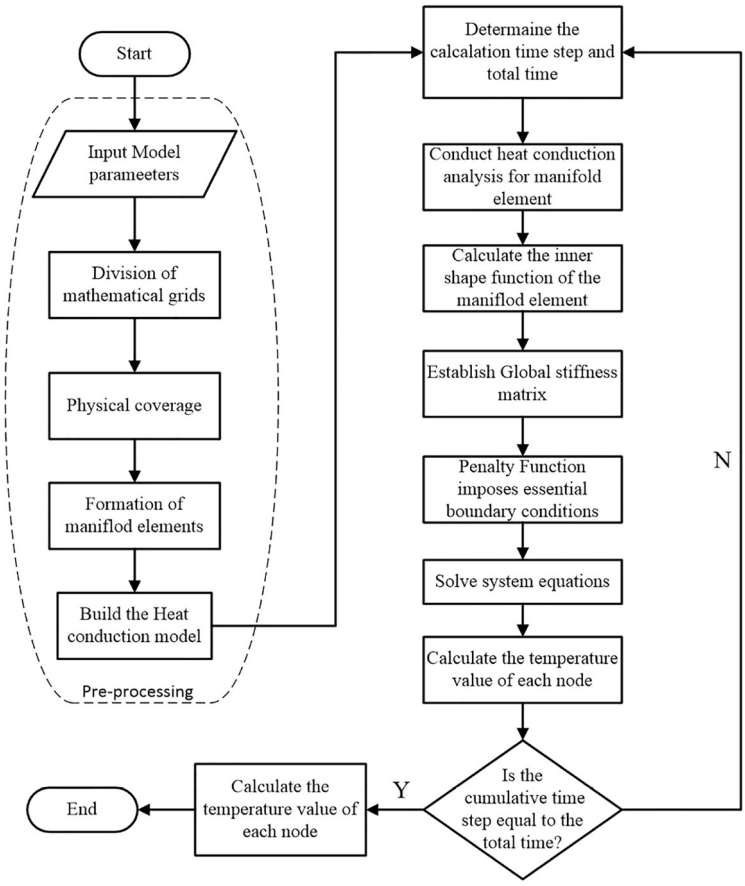

Figure 3 Flow of the solution of calculating 3D TRHC problems.

hexahedron as the mathematical mesh. When use the mesh density of 0.25 m (ME-0.25 m) it means the edge length of the cubic element is 0.25 m. In order to verify the reliability of the calculation results, we also use FEM program for finite element analysis, the calculation element is DC3D8, and the calculation time step is same as the 3D-NMM. The following examples are the same and will not be explained later.

The temperature in the x-direction in the model is analytically calculated as follows:

$$T(x) = \frac{T_a - T_b}{10l}x + T_b. \tag{35}$$

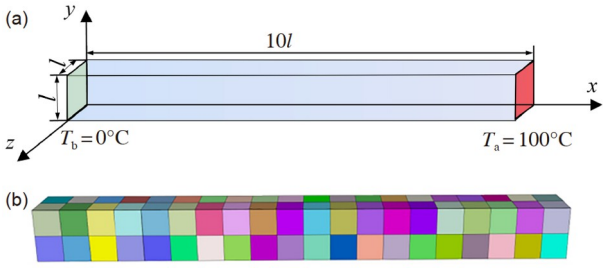

Figure 4 Model for the calculation of one-dimensional long-rod. (a) Geometric model; (b) numerical model.

The analytical and numerical solutions to the SSHC problems for the long rod were obtained with the central axis of the long-rod as the monitoring profile, as illustrated in Figure 5. The calculated results of 3D NMM and FEM are consistent with the analytical solution, indicating that 3D NMM can be used to effectively solve SSHC problems.

Figure 6 shows the error rate with different penalty value. As can be seen from the figure, the error rate gradually decreases as the penalty value increases. When the penalty value was taken as 1×10^5, its maximum error rate does not exceed 1.6%. In addition, when the penalty value was taken as 1×10^7, its maximum error rate does not exceed 0.0162%, which can be considered as the ideal calculation result. As can be seen from the figure, the larger the penalty value the higher the accuracy of its calculation. However, due to the problem of penalty method itself, its penalty value cannot be too large, otherwise it will easily lead to the pathology of matrix. Thus, the initial penalty value can be selected according to eq. (16) and subsequently adjusted flexibly according to the calculation result.

In order to discuss the mesh density and the convergence of 3D-NMM, a penalty value of 1×10^7 was chosen for the calculation. Figure 7 shows the error rate with different mesh

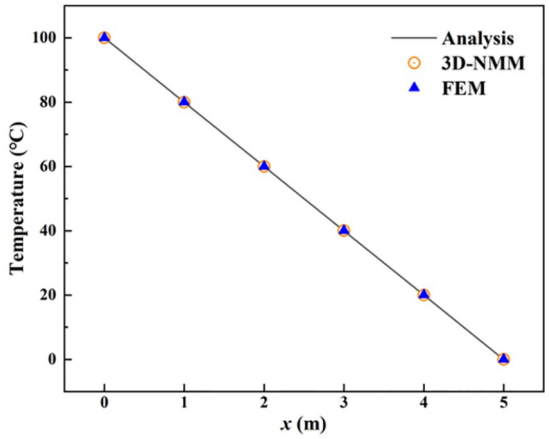

Figure 5 Comparison of analytical and numerical results of SSHC problems.

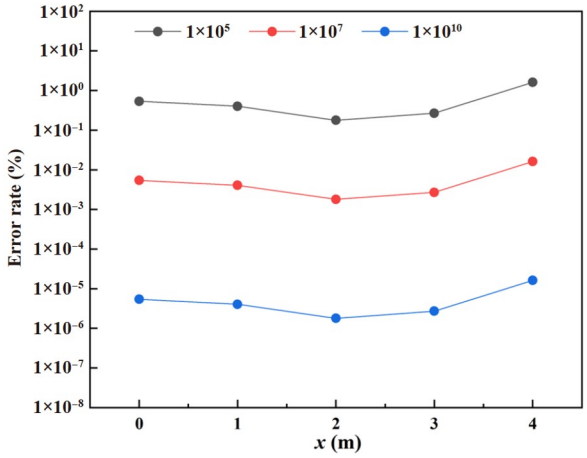

Figure 6 The error rate with different penalty value.

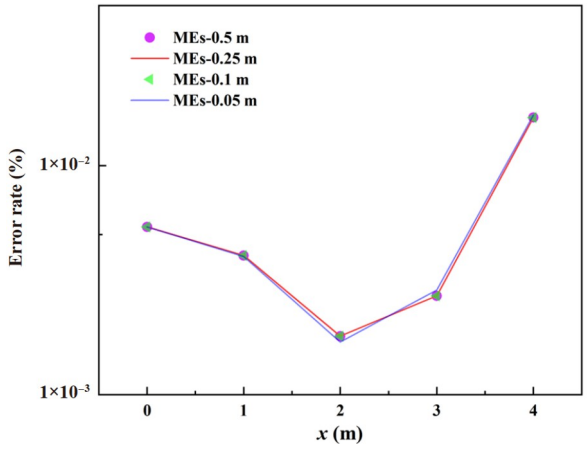

Figure 7 The error rate with different mesh density.

density. It can be concluded from Figure 7 that the calculation results of 3D-NMM are less affected by the mesh density, and the error rate does not change so much when the mesh density increases by a factor of 10. Therefore, the 3D-NMM has better computational accuracy and convergence.

Figure 8(a) and (b) illustrate the numerical calculation results of 3D NMM and FEM. The temperature field distributions in the temperature contour plots obtained through 3D NMM and FEM were similar. The accuracy of the temperature contour plot was also verified using the monitoring data displayed in Figure 5. The results indicated that the proposed 3D NMM algorithm is feasible, accurate, and effective for solving 3D heat conduction problems.

The time domain was discretized for the SSHC problem to verify the accuracy of the 3D NMM for solving TRHC problems. According to the time step setting process described in Section 3.4, the time step was fixed at 5×10^5 s for a total of 20 steps. A steady state was reached at 7.5×10^6 s.

The SSHC problem can be considered as the final result of the transient calculation. Figure 9 displays the curve of monitoring points changes in temperature with time under the 3D transient heat conduction. The obtained 3D-NMM

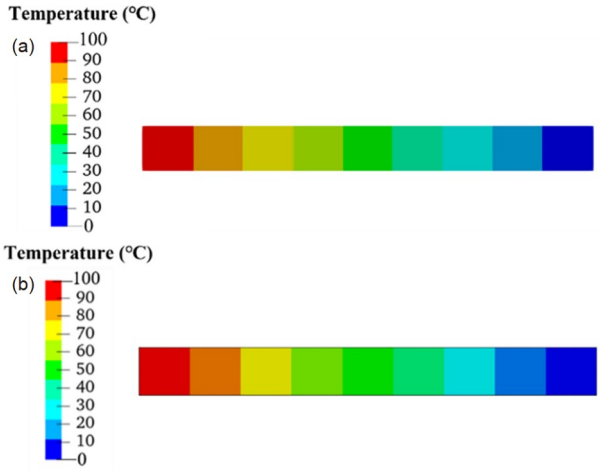

Figure 8 Comparison of 3D-NMM and FEM steady-state temperature contours. (a) 3D-NMM; (b) FEM.

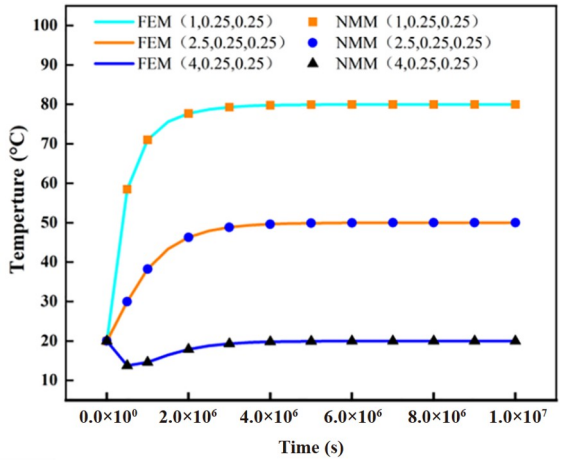

Figure 9 Transient temperature variation curve of monitoring points obtained using 3D-NMM and FEM.

calculation results are compared with the FEM calculation results. The curves obtained using 3D-NMM and FEM are in good agreement, indicating it is feasible to extend 3D-NMM to the TRHC problem and can help derive solutions to thermal fracture problems.

4.2 Rectangular rock specimen

As illustrated in Figure 10, the length, width, and height of a granite rock body which was assumed to be an isotropic material were a, b, and c, respectively. The thermodynamic parameters of the granite body were as follows: k=2.7 W/(m °C), c=0.92 kJ/(kg °C), and ρ = 2.7 g/cm^3. In addition, the upper and lower fixed-temperature boundary conditions were as follows: T_a = 100°C, and T_b = 0°C. The granite rock did not contain any heat source, and the temperatures at the left and right boundaries were 0°C. The specific geometric model and numerical model are displayed in Figure 8.

According to ref. [43], the analytical solution was obtained using the following expression:

$$T(x,y)=\frac{2T_a}{\pi}\sum_{n=1}^{\infty}\frac{[-(-1)^n+1]}{n}\frac{\sin\lambda_n y}{\sin\lambda_n b}\sin\lambda_n x,\left(\lambda_n=\frac{n\pi}{a}\right). \tag{36}$$

The model was constructed in the Cartesian coordinate system with the following dimensions: a = 2 m, b = 4 m, and c = 2 m. To examine the computational effectiveness and accuracy of the software, different mesh densities were employed for computations, and the results were compared with the analytical solution. The mesh density were 0.5 m (ME-0.5 m), 0.25 m (ME-0.25 m), and 0.1 m (ME-0.1 m), and the numbers of MEs were 2251024, and 18081, respectively. The steady state was reached at 1.5×10^7 s, as mentioned in Section 3.4. The discretized numerical computational model is displayed in Figure 11.

The middle plane of the model was chosen as the monitoring plane, and the contour plot represented the temperature variation inside the rectangular rock. As shown in Figure 12, it is the steady-state temperature contour plot calculated by 3D-NMM (MEs-0.25m) and the steady-state temperature contour plot of FEM at a grid density of 0.1 m. The two contour plots were consistent, indicating that 3D-NMM can achieve the same calculation effect as FEM at a lower grid density and the results were consistent with the heat conduction law, which indicates that 3D-NMM is accurate and feasible in calculating such problems.

Three points (1, 1, 1) (1, 2, 1), and (1, 3, 1) on the mid-plane were used as monitoring points to analyze the temperature variations in transient and steady-state cases. Figure 13 displays the variations in temperature and different mesh densities at different monitoring points calculated using 3D-NMM for the temperature field problem. For various grid densities, the 3D-NMM simulation results were consistent with the analytical solution. Furthermore, with the increase in grid density, the numerical solution becomes closer to the analytical solution. For ME-0.25 m, the error between the temperature values at each monitoring point and the analytical solution did not exceed 0.2°C.

Figure 14 displays the Error rate of steady-state temperature with different mesh densities. It can be seen from the figure that the accuracy of the 3D-NMM calculation results

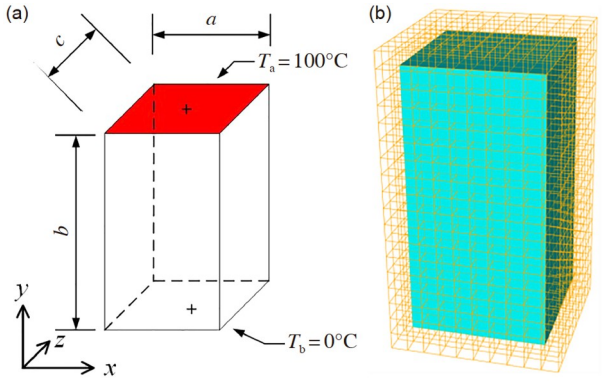

Figure 10 Model for the rectangular rock specimen. (a) Geometric model; (b) numerical model (MEs-0.25 m).

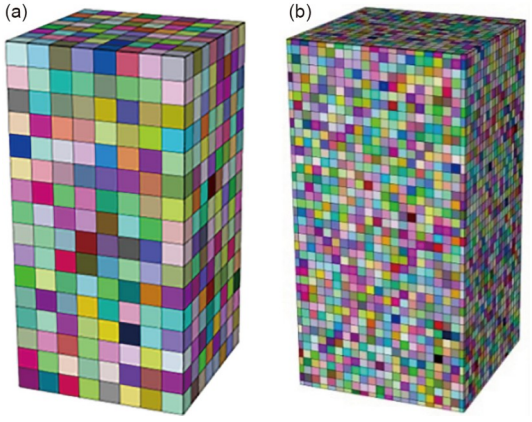

Figure 11 3D-NMM computational model with different grid densities. (a) MEs-0.25 m; (b) MEs-0.1 m.

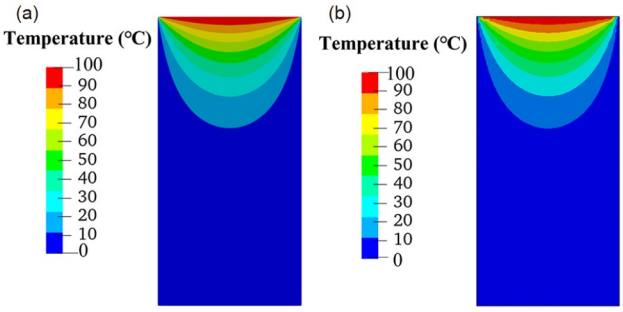

Figure 12 Comparison of 3D-NMM and FEM steady-state temperature clouds. (a) 3D-NMM; (b) FEM.

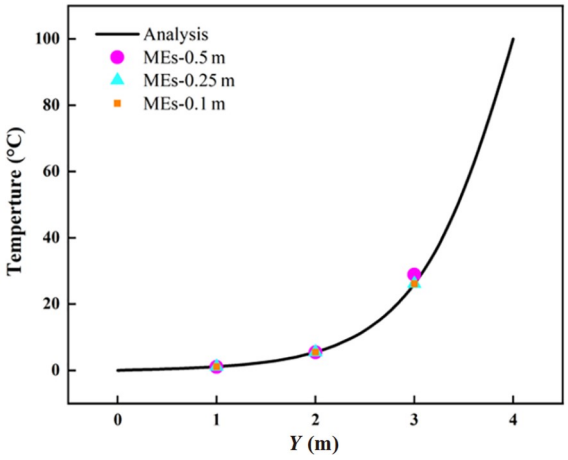

Figure 13 Simulation results of steady-state temperature with different mesh densities.

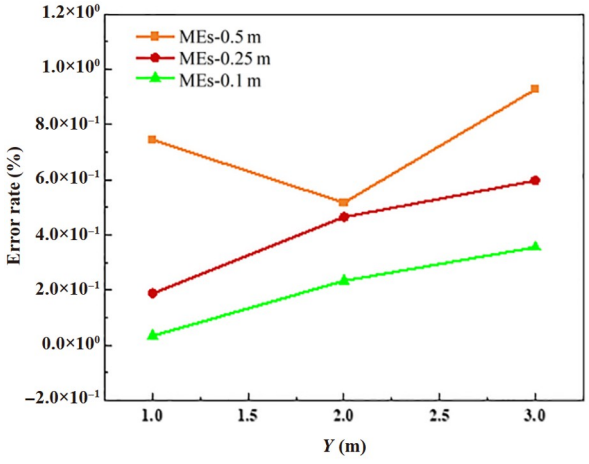

Figure 14 Error rate of steady-state temperature with different mesh densities.

is higher with the increase of the mesh density. When the mesh density is 0.1 m its error does not exceed 0.36%.

As displayed in Figure 15, the model reached the steady state at 1.5×10^7 s, thereafter, the temperature field unaffected by time. In addition, the calculation results were consistent with the finite element calculation results in the time domain, indicating 3D-NMM can be used to solve 3D transient heat conduction problems with high accuracy.

4.3 High-temperature tunnel

A large secondary project located in the Gaizi River Basin on the Pamir Plateau in Xinjiang, China, is the only water conservancy control hub for the gradient development of the Gaizi River Basin. During the excavation, the maximum ambient temperature at the palm face reached 67°C, the maximum temperature inside the cave exceeded 105°C, while the overwater temperature during the operation period was as low as 0–5°C [44]. The surrounding rock was a Class

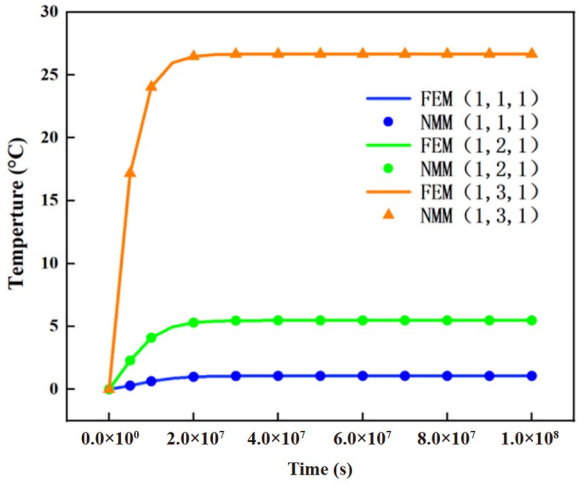

Figure 15 Comparison of the transient temperature values calculated using 3D-NMM with FEM results.

III rock composed of mica-quartz schist interspersed with graphite schist. According to the literature, the ground temperature in the project increased because of uneven heat conduction due to the large difference in the burial depth of each section. To analyze the temperature conduction process in high-temperature tunnels, a 3D-NMM calculation model was established using the FDEM [45,46] calculation method. The thermodynamic parameters were as follows: k= 2.2 W/(m °C), c=1.2 kJ/(kg °C) and ρ=2.6 g/cm^3.

The calculation model is displayed in Figure 16(a). The dimensions of the surrounding rock in the model were 120 m × 120 m × 10 m. The radius of tunnel was R_0 = 4.3 m. The vertical axis, where the point (0, 4.3, 5) was located on the tunnel was selected as the monitoring line. Figure 16(b) illustrates the numerical model after discretization using the preprocessing tool of 3D-NMM with a mathematical mesh density of 2 m, generating a total of 17980 MEs. The tunnel was fixed as a low-temperature boundary, and the surrounding rock was fixed as an initial high-temperature boundary. To analyse the distribution of the temperature field, the low-temperature boundary was fixed at 5°C, 10°C, 20°C, and 30°C and the high-temperature boundary was fixed at 60°C, 70°C, 80°C, and 90°C. To verify the accuracy of 3D-NMM, the low-temperature boundary was fixed at 30°C and the high-temperature boundary was fixed at 80°C.

Figure 17 displays the curves of temperature variations of 3D-NMM and FDEM at different positions. The calculated temperature of the surrounding rock increased nonlinearly with the increase in the radius of the surrounding rock. The farther away the surrounding rock is from the centre of the tunnel circle, the higher the temperature of the surrounding rock. The closer the surrounding rock is to the centre of the tunnel, the lower the temperature of the surrounding rock. In addition, the results obtained using the proposed numerical algorithm proposed in this paper agree well with the FDEM

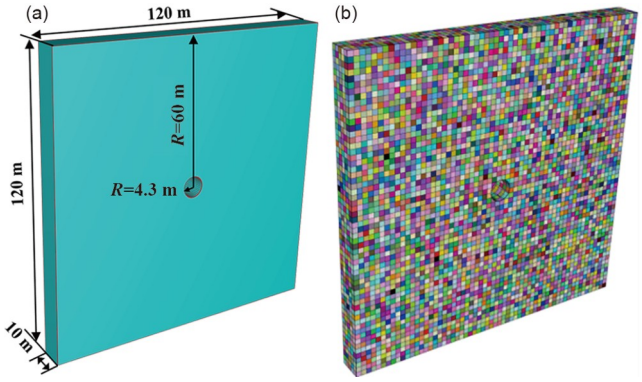

Figure 16 Calculation model of the high-temperature tunnel. (a) Geometric model; (b) numerical model (MEs-2 m).

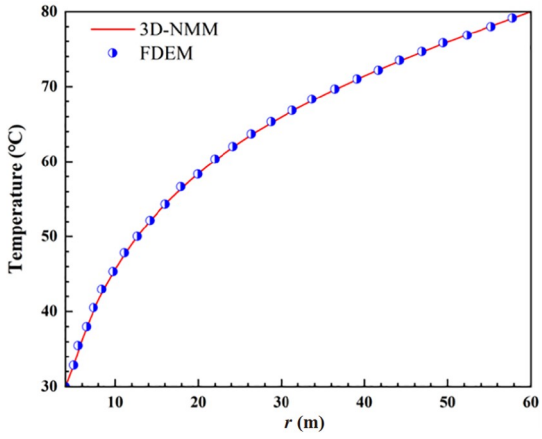

Figure 17 Curves displaying temperature variations at different locations calculated using 3D NMM and FDEM.

calculation results, which again verifie that the algorithm achieves good computational results for both problems with and without analytic solutions. Thus, this method is feasible for solve the heat conduction problems with high accuracy.

Figure 18 displays a contour plot of the temperature distribution in the high-temperature tunnel surrounding rock. After excavation, the high-temperature tunnel was in contact with the external environment, thereby causing the air-contact part of the tunnel to gradually cool down to normal temperature, while the temperature of the distal surrounding rock still maintained the high temperature. Therefore, the temperature in the surrounding rock in space had a gradient distribution

Figure 19 illustrates the relationship between the temperature of the surrounding rock and the ambient temperature of the tunnel under fixed external boundary conditions of 80°C, so that the ambient temperatures of the tunnel are 5°C, 10°C, 20°C, and 30°C, respectively. With the gradual increase in the ambient temperature of the tunnel, the temperature of the surrounding rock at the same distance from the centre of the tunnel circle increased. The temperature distribution increased nonlinearly from the part of the tunnel

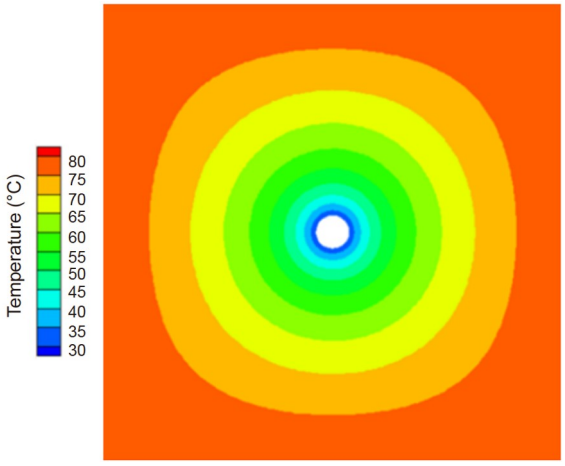

Figure 18 Temperature distribution contour plot of a high-temperature tunnel.

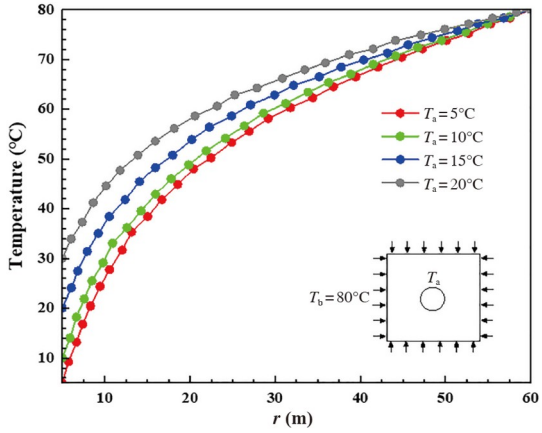

Figure 19 Variations in the ambient temperature at a fixed surrounding rock temperature.

in contact with air to the far side of the surrounding rock; the lower the ambient temperature, the steeper the curve, and the higher the ambient temperature of the tunnel, the flatter the curve, indicating that the heat transfer was influenced by the temperature gradient.

Figure 20 displays the variation curves of heat transfer in the surrounding rock at different temperature boundaries for a fixed tunnel ambient temperature of 30°C and external boundary conditions of 60°C, 70°C, 80°C, and 90°C. The higher the temperature of the surrounding rock, the steeper the curve, indicating that the temperature of the surrounding rock had a more notable influence on heat transfer. Thus, a reasonable cave temperature should be selected to ensure the stability of the surrounding rock. The temperature distribution in the surrounding rock in a homogeneous high-temperature tunnel was closely related to the temperature inside the tunnel, the initial temperature of the surrounding rock, and other factors. In actual projects, the initial temperature of the tunnel should be controlled to prevent the redistribution of stress caused by the redistribution of the temperature field.

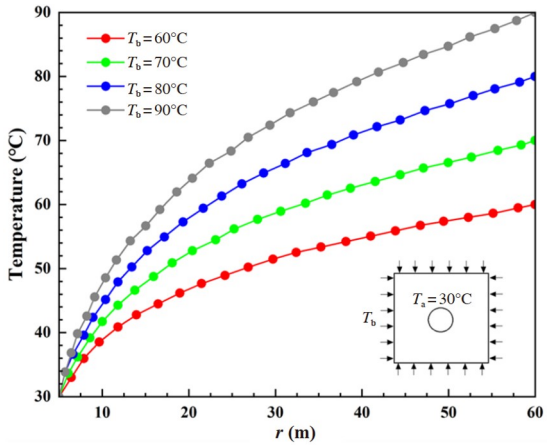

Figure 20 Variation of the surrounding rock temperature under a define ambient temperature.

This can affect the quality of the project and the safety of people's lives and properties.

4.4 Nuclear waste storage example

In this study, we examined a nuclear waste storage facility which was 4 m in length and 4 m in width, with a central storage hole having a length of 0.4 m and a width of 0.4 m. This calculation assumes an isotropic material and uses granite as the study medium. The thermodynamic parameters of granite were as follows: k=2.7 W/(m °C), c=0.92 kJ/(kg °C), and ρ = 2.7g/cm^3. For the calculations, the mid-plane of the storage cavern with the nuclear waste stack was selected as the calculation profile, and the length of the longitudinal extension was fixed at 0.4 m to calculate the changes in temperature change in the surrounding rock under the action of the nuclear waste stack. The inner and outer surface temperatures, T_a = 200°C and T_b = 20°C, respectively, and the initial temperature of the model was T_0 = 20°C.

In the proposed model, the mesh densities of ME-0.1 and ME-0.05 were selected to generate 6336 and 50688 MEs, respectively. The temperature distribution in this model was selected using a 3D-NMM, and compared with the FEM calculation results. Five monitoring points were selected to analyse the variations in temperature with time, the coordinates of the points were (2, 1.7, 0.2), (2, 1.5, 0.2), (2, 1, 0.2), (2, 0.5, 0.2), and (2, 0.2, 0.2). Figure 21 displays the model for the calculation of nuclear waste storage.

Figure 22 shows the comparison curves of the calculation results using 3D-NMM and FEM, which uses the numerical solution with a grid density of 0.01 m as the reference solution. According to the time step setting process described in Section 3.4, the time step was fixed at 5×10^6 s for a total of 20 steps. A steady state was reached at 7.5×10^7 s, and the calculation results show that the 3D-NMM has good computational results in calculating this model and has a high

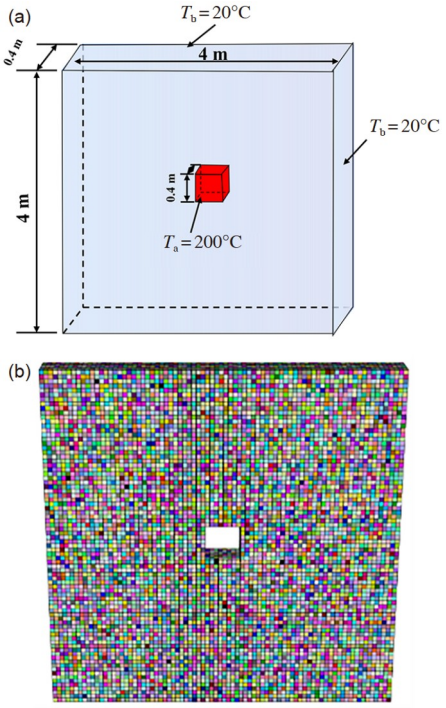

Figure 21 Model for the calculation of nuclear waste storage. (a) Geometric Model; (b) numerical model.

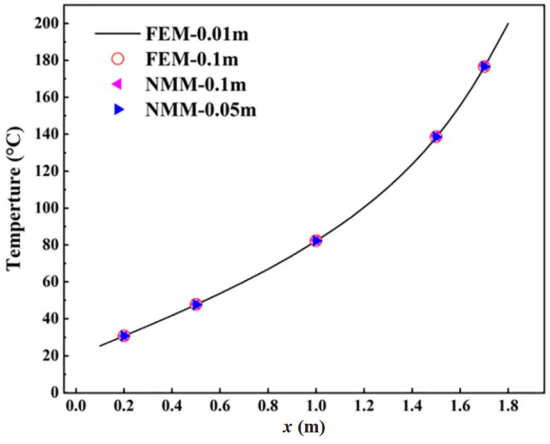

Figure 22 Comparison of the curves plotted according to the results of 3D-NMM and FEM (t=7.5×10^7 s).

agreement with the corresponding other numerical methods.

As illustrated in Figure 23, the curves plotted according to the 3D NMM transient calculation results compared with those obtained using the FEM. The curve gradually approached the steady-state value with the progression of time steps. In addition, the transient calculation results obtained using the 3D NMM were consistent with those obtained using the FEM, indicating that the 3D NMM can be used to accurately solve the transient problem.

Figure 24 illustrates the steady-state temperature plot of the 3D NMM and the FEM. The results of the 3D NMM were consistent with those of the FEM. In addition, the heat

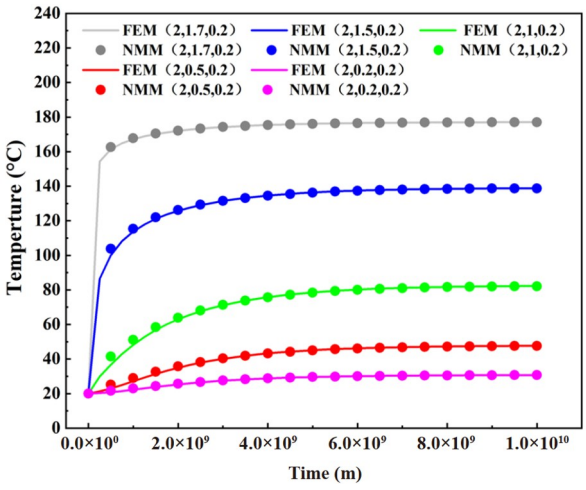

Figure 23 Comparison of the curves plotted using the transient calculation results of 3D NMM and FEM.

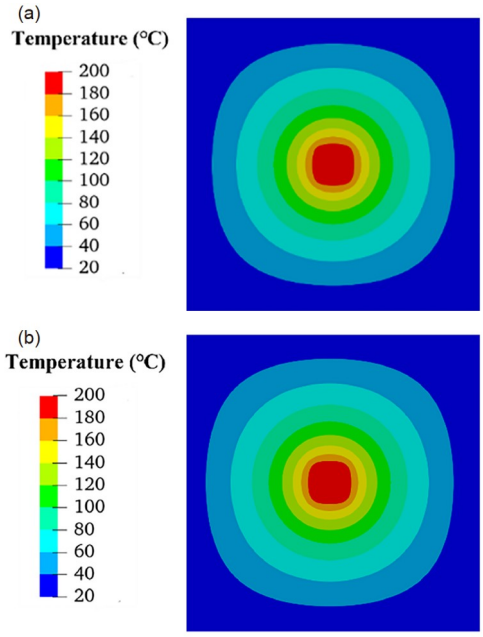

Figure 24 Steady-state temperature contour plot for nuclear waste storage. (a) 3D-NMM; (b) FEM.

conduction effect of the nuclear waste storage was observed roughly within a 4 m × 4 m × 4 m space, and the conduction was gradual from the centre along the surrounding boundary with a centrosymmetric distribution. Therefore, the heat radiated outward from the nuclear waste storage chamber of the deep rock mass was mainly concentrated in a space with a side length of 4 m and had a limited range of influence. Moreover, no large-scale heat transfer was observed in the deep rock mass.

4.5 Cuboid plate with two cracks

In this example, a cuboid plate with a circular hole in the middle and two predetermined cracks was examined. Figure 25 shows the geometric model and numerical model of cuboid plate with two cracks. In order to better compare with the existing literature, the corresponding boundary conditions in the case of ref. [28] are selected for analysis, which can be considered to consistent with the two-dimensional heat conduction mode. In the calculation, the length, width, and height of the rectangular cuboid plate are 2 m×2 m×0.5 m, the crack length is a=0.3 m, and the radius of the circular hole is R=0.2 m. The initial conditions were as follows: the upper and lower boundaries of the model had fixed temperatures: T_a = 100°C, and T_b = 0°C; the left and right boundaries were adiabatic; no heat source was present inside or outside the square plate.

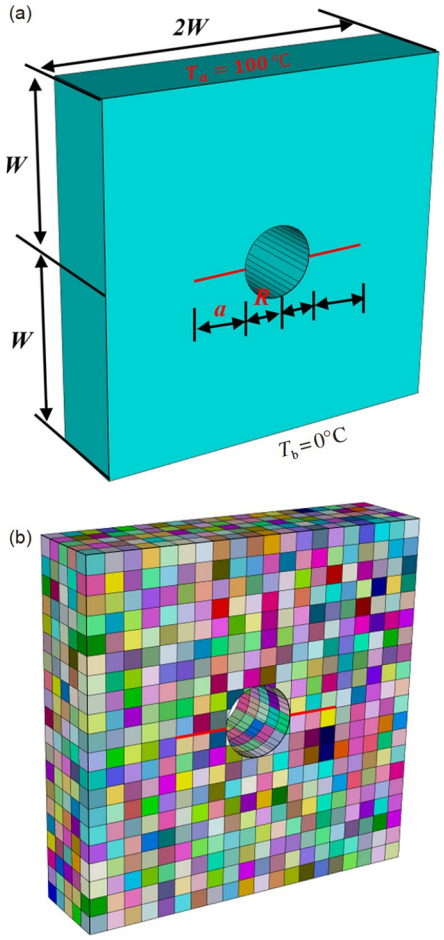

Figure 25 Model for the calculation of square plate with two cracks. (a) Geometric model; (b) numerical model (MEs-0.1 m).

The contour plot of the steady state calculation is displayed in Figure 26, and is consistent with the contour plot obtained by Zhang et al. [28]. The cracks effectively impeded heat movement inside the rock mass, indicating that the method proposed in this study is suitable for accurately simulating heat conduction problems with fractures. The model can be used as an initial model for thermal fractures and can thus

provide a basis for subsequent research.

Figure 27 shows the contour plot of the effect of different crack lengths on heat conduction. From the contour plot, it can see that as the crack length increases, the heat conduction is blocked to a larger area. The heat conduction shows an obvious jump on both sides of the crack, and the longer the crack, the greater the temperature gap between the two sides of the crack. As a result, cracks can lead to an increase in temperature gradients during heat conduction, which can lead to the accumulation of thermal stresses and have an impact on engineering stability. The example shown in this paper is a preliminary exploration of the three-dimensional thermal fracture problem, which will be investigated in depth subsequently.

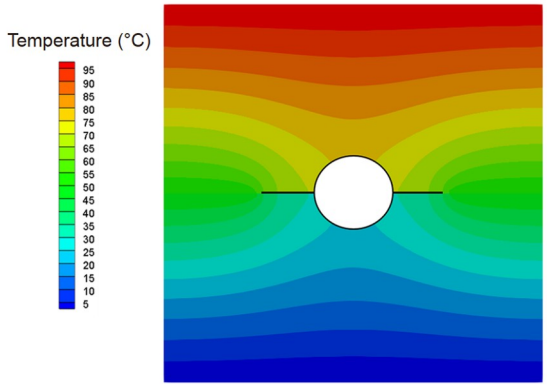

Figure 26 Steady-state temperature cloud plot for the square plate with two cracks (R=0.2 m, a=0.3 m).

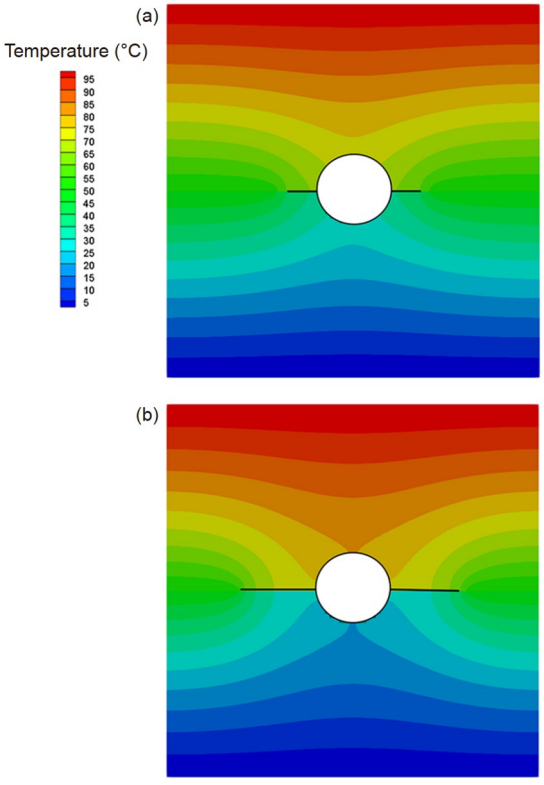

Figure 27 The contour plot of the effect of different crack lengths on heat conduction. (a) R=0.2 m, a=0.2 m; (b) R=0.2 m, a=0.4 m.

5 Conclusions

NMM has attracted considerable attention from researchers in the last three decades. With advantages of such as low grid dependence, high computational accuracy, high solution speed, and wide applicability, the NMM is used in geotechnical, mining, and physical exploration fields. In this study, based on the research of 3D-NMM, we extended 3D-NMM to simulate steady-state and transient heat conduction problems, and the system equations are constructed by Galerkin variational method, and the boundary conditions are imposed by the penalty function method. The key conclusion can be summarized as follows.

(1) An algorithm for the generation of 3D manifold elements (MEs) was established, and a Galerkin weighted residual value method was used to derive the governing equation. In addition, the boundary conditions and variational problems of the three-dimensional steady-state and transient temperature fields were derived from the basic differential equations.

(2) For the surface integral problem in three-dimensional space, we obtained exact boundary integral for the heat conduction problem by projecting a polygon in three-dimensional space onto the coordinate plane and by subsequently using a two-dimensional simplex integral to perform the calculation.

(3) Unlike the SSHC problem, the TRHC problem was solved by adding a time derivative factor to derive the overall equation. Furthermore, the time step setting in the calculation module was updated to illustrate the effectiveness and high accuracy of 3D-NMM in solving transient heat conduction problems through transient and steady-state analyses.

(4) Using the hexahedral FE-mesh as the mathematical mesh notably simplified the pre-processing and shape function construction problems. As an advanced numerical computation method, the NMM with two sets of meshes has an irreplaceable advantage in dealing with the fracture solution process. The method proposed in this study can be used to accurately solve heat conduction problems and the results obtained are consistent with the analytical solution and FEM, which can provide a basis for the subsequent development of thermal coupling problems.

This work was supported by the National Natural Science Foundation of China (Grant Nos. 42277165, 41920104007, and 41731284), the Fundamental Research Funds for the Central Universities, China University of Geosciences (Wuhan) (Grant Nos. CUGCJ1821 and CUGDCJJ202234), and the National Overseas Study Fund (Grant No. 202106410040).

1 Tan F, Tong D, Liang J, et al. Two-dimensional numerical manifold method for heat conduction problems. Eng Anal Bound Elem, 2022, 137: 119–138
2 Han Z Y, Li D Y, Li X B. Effects of axial pre-force and loading rate on Mode I fracture behavior of granite. Int J Rock Mech Min, 2022, 157: 105172
3 Fan L F, Yi X W, Ma G W. Numerical manifold method (NMM) simulation of stress wave propagation through fractured rock mass. Int J Appl Mech, 2013, 05: 1350022
4 Fan L, Gao J, Du X, et al. Spatial gradient distributions of thermal shock-induced damage to granite. J Rock Mech Geotechnical Eng, 2020, 12: 917–926
5 Fan L F, Wu Z J, Wan Z, et al. Experimental investigation of thermal effects on dynamic behavior of granite. Appl Thermal Eng, 2017, 125: 94–103
6 Zhang H H, Han S Y, Fan L F, et al. The numerical manifold method for 2D transient heat conduction problems in functionally graded materials. Eng Anal Bound Elem, 2018, 88: 145–155
7 Bruch J C, Zyvoloski G. Transient two-dimensional heat conduction problems solved by the finite element method. Int J Numer Meth Engng, 1974, 8: 481–494
8 Reddy J N, Gartling D K. The Finite Element Method in Heat Transfer and Fluid Dynamics. Boca Raton: CRC Press, 2010
9 Brian P L T. A finite-difference method of high-order accuracy for the solution of three-dimensional transient heat conduction problems. AIChE J, 1961, 7: 367–370
10 Wang C C. Application of the maximum principle for differential equations in combination with the finite difference method to find transient approximate solutions of heat equations and error analysis. Numer Heat Transfer Part B-Fundamentals, 2009, 55: 56–72
11 Li W, Yu B, Wang X, et al. A finite volume method for cylindrical heat conduction problems based on local analytical solution. Int J Heat Mass Transfer, 2012, 55: 5570–5582
12 Liu D, Cheng Y M. The interpolating element-free Galerkin method for three-dimensional transient heat conduction problems. Results Phys, 2020, 19: 103477
13 Wrobel L C, Brebbia C A. The boundary element method for steady state and transient heat conduction. Numerical Methods in Thermal Problems, 1979. 58–73
14 Gao X W. A meshless BEM for isotropic heat conduction problems with heat generation and spatially varying conductivity. Int J Numer Meth Engng, 2006, 66: 1411–1431
15 Shi G H. Manifold method of material analysis. In: Proceedings of the Transactions of the 9th Army Conference On Applied Mathematics and Computing. Minneapolis, 1991. 57–76
16 Ma G, An X, He L. The numerical manifold method: A review. Int J Comput Methods, 2010, 07: 1–32
17 Yang S, Ma G, Ren X, et al. Cover refinement of numerical manifold method for crack propagation simulation. Eng Anal Bound Elem, 2014, 43: 37–49
18 Liu F, Xia K. Structured mesh refinement in MLS-based numerical manifold method and its application to crack problems. Eng Anal Bound Elem, 2017, 84: 42–51
19 Liu F, Zhang K, Xu D D. Crack analysis using numerical manifold method with strain smoothing technique and corrected approximation for blending elements. Eng Anal Bound Elem, 2020, 113: 402–415
20 Chen G, Ohnishi Y, Ito T. Development of high-order manifold method. Int J Numer Meth Engng, 1998, 43: 685–712
21 Zhang H H, Liu S M, Han S Y, et al. Modeling of 2D cracked FGMs under thermo-mechanical loadings with the numerical manifold method. Int J Mech Sci, 2018, 148: 103–117
22 Wu Z, Sun H, Wong L N Y. A cohesive element-based numerical manifold method for hydraulic fracturing modelling with voronoi grains. Rock Mech Rock Eng, 2019, 52: 2335–2359
23 Yang Y, Chen T, Zheng H. Mathematical cover refinement of the numerical manifold method for the stability analysis of a soil-rock-mixture slope. Eng Anal Bound Elem, 2020, 116: 64–76
24 Chen T, Yang Y, Zheng H, et al. Numerical determination of the effective permeability coefficient of soil-rock mixtures using the numerical manifold method. Int J Numer Anal Methods Geomech, 2019, 43: 381–414
25 He J, Liu Q, Wu Z, et al. Modelling transient heat conduction of granular materials by numerical manifold method. Eng Anal Bound Elem, 2018, 86: 45–55
26 He J, Liu Q, Wu Z, et al. Geothermal-related thermo-elastic fracture analysis by numerical manifold method. Energies, 2018, 11: 1380
27 Zhang H H, Liu S M, Han S Y, et al. The numerical manifold method for crack modeling of two-dimensional functionally graded materials under thermal shocks. Eng Fract Mech, 2019, 208: 90–106
28 Zhang H H, Ma G W, Ren F. Implementation of the numerical manifold method for thermo-mechanical fracture of planar solids. Eng Anal Bound Elem, 2014, 44: 45–54
29 Gao H, Wei G. Complex variable meshless manifold method for transient heat conduction problems. Int J Appl Mech, 2017, 09: 1750067
30 Zhang L, Guo F, Zheng H. The MLS-based numerical manifold method for nonlinear transient heat conduction problems in functionally graded materials. Int Commun Heat Mass Transfer, 2022, 139: 106428
31 Tan F, Tong D F, Yi X W, et al. 3D numerical manifold element generation software. Version 1.0. Wuhan (CN): National Copyright Administration. 2021
32 Sun L, Zhao G, Ma X. Quality improvement methods for hexahedral element meshes adaptively generated using grid-based algorithm. Int J Numer Meth Engng, 2012, 89: 726–761
33 He L, An X M, Ma G W, et al. Development of three-dimensional numerical manifold method for jointed rock slope stability analysis. Int J Rock Mech Min Sci, 2013, 64: 22–35
34 Yang Y T, Li J F. A practical parallel preprocessing strategy for 3D numerical manifold method. Sci China Tech Sci, 2022, 65: 2856–2865
35 Liu F, Zhang K, Liu Z. Three-dimensional MLS-based numerical manifold method for static and dynamic analysis. Eng Anal Bound Elem, 2019, 109: 43–56
36 Liang J, Tong D, Tan F, et al. Two-Dimensional magnetotelluric modelling based on the numerical manifold method. Eng Anal Bound Elem, 2021, 124: 87–97
37 Zheng H, Xu D. New strategies for some issues of numerical manifold method in simulation of crack propagation. Int J Numer Meth Engng, 2014, 97: 986–1010
38 Yang Y, Tang X, Zheng H, et al. Three-dimensional fracture propagation with numerical manifold method. Eng Anal Bound Elem, 2016, 72: 65–77
39 Mills A F. Heat Transfer. Boca Raton: CRC Press, 1992
40 Logan D L. A First Course in the Finite Element Method. Hoboken: John Wiley & Sons, 2007
41 Lin S Z. Recursive formula for simplex integration. J Yangtze River Sci Res Inst, 2005, 22: 32
42 Wang X, Wu W, Zhu H, et al. Three-dimensional discontinuous deformation analysis derived from the virtual work principle with a simplex integral on the boundary. Comput Geotechnics, 2022, 146: 104710
43 Huang H C, Wang Q L. Finite Element Analysis of Heat Conduction Problems. Beijing: Science Press, 2011
44 Huang Y, Jiang H. Analysis of characteristics of plastic zone and mechanical properties of anchor structure in hydraulic tunnels with high ground temperature. Eur J Comput Mech, 2021, 481–500
45 Yan C, Wei D, Wang G. Three-dimensional finite discrete element-based contact heat transfer model considering thermal cracking in continuous–discontinuous media. Comput Methods Appl Mech Eng, 2022, 388: 114228
46 Wang T, Yan C, Wang G, et al. Numerical study on the deformation and failure of soft rock roadway induced by humidity diffusion. Tunnelling Underground Space Tech, 2022, 126: 104565